Chemical Science

ROYAL SOCIETY OF CHEMISTRY

EDGE ARTICLE

View Article Online
View Journal | View Issue

Cite this: *Chem. Sci.*, 2024, **15**, 13841

All publication charges for this article have been paid for by the Royal Society of Chemistry

Received 3rd June 2024
Accepted 30th July 2024

DOI: 10.1039/d4sc03642e

rsc.li/chemical-science

More is different: progressive β-thiolation induced-porphyrin aggregation switches singlet oxygen photosensitization†

Mengliang Zhu,‡[ab] Hang Zhang,‡[a] Yuhang Yao,‡[a] Mingpu Wen,[c] Guangliu Ran,[d] Yi Yu,[a] Ruijing Zhang,[a] Xing-Jie Liang,[be] Jing Zhang,[c] Wenkai Zhang *[d] and Jun-Long Zhang *[a]

Incorporating sulfur atoms into photosensitizers (PSs) has been well-established to populate triplet states and increase singlet oxygen ($^1O_2$) production when exposed to light. In this work, we found that progressive thiolation of porphyrin β-periphery does promote intersystem crossing (ISC) between triplets and singlets, as seen in the excited state dynamics in dichloromethane or PS nanoparticles in water. However, in the latter case, more sulfur substitution deactivates $^1O_2$ photosensitization, in contrast to the expected trend observed in dichloromethane. This observation was further supported by photocytotoxicity studies, where $^1O_2$ photosensitization was switched off in living cells and multicellular spheroids despite being switched on in *in vivo* mice models. To understand the inconsistency, we performed molecular dynamics simulation and time-dependent density functional theory calculations to investigate possible aggregation and related excited states. We found that the extent of thiolation could regulate molecular packing inside nanoparticles, which gradually lowers the energy levels of triplet states even lower than that of $^1O_2$ and, in turn, alters their energy dissipation pathways. Therefore, this study provides new insights into the design of metal-free PSs and sheds light on the excited state dynamics in aqueous media beyond the molecular level.

Introduction

Photodynamic therapy (PDT), which relies on oxygen activation upon light irradiation, has been an emerging treatment for tumors and dermatological conditions due to its inherent advantages such as high selectivity, non-invasiveness, and therapeutic efficacy.[1–4] Typically, excitation of the photosensitizer (PS) leads to a singlet excited state which is subsequently converted to the triplet state through intersystem crossing (ISC), and it finally reacts with the surrounding molecular oxygen ($^3O_2$) to produce singlet oxygen ($^1O_2$).[5–8] Thus, the excited state dynamics of PS is critical in determining oxidative events, cytotoxicity, and even death.[9–11] Molecular engineering of PSs to modulate the excited state dynamics has been established; for example, the efficiency of the ISC process can be enhanced by introducing the heavy-atom effect,[12,13] reducing the energy gap (ΔE_{ST}) between the lowest singlet (S_1) and the lowest triplet (T_1),[14,15] or increasing the rigidity of PSs,[16,17] according to Fermi's Golden rule.[18] On the other hand, increasing attention has recently been devoted to molecular self-assembly or aggregate formation, demonstrating distinct optoelectronic, chemical, and biological properties from single molecules.[19–22] These studies open an opportunity, namely "more is different", to guide the molecular engineering of PSs for biomedicine purposes.[23–26]

Introducing sulfur atoms into the backbone of PSs is promising to enhance ISC and populate the triplet states, probably circumventing the heavy metal toxicity.[27] Yoon, Xiao, Lu, and others have demonstrated that thiocarbonyl PSs are readily obtained by the reaction of Lawesson's reagent with carbonyl PS analogs.[28–31] Theoretical calculations suggested that sulfur substitution significantly promotes the spin–orbit coupling (SOC), narrows ΔE_{ST} between singlet and triplet states, and thus enhances the ISC rate.[32,33] Despite the effectiveness of

[a]*Beijing National Laboratory for Molecular Sciences, College of Chemistry and Molecular Engineering, Peking University, Beijing 100871, P. R. China. E-mail: zhangjunlong@pku.edu.cn*

[b]*CAS Key Laboratory for Biomedical Effects of Nanomaterials and Nanosafety, CAS Center for Excellence in Nanoscience, National Center for Nanoscience and Technology of China, Beijing 100190, P. R. China*

[c]*College of Materials Science and Opto-Electronic Technology, University of Chinese Academy of Sciences, Beijing 100049, P. R. China*

[d]*Center for Advanced Quantum Studies, Department of Physics and Applied Optics Beijing Area Major Laboratory, Beijing Normal University, Beijing 100875, P. R. China. E-mail: wkzhang@bnu.edu.cn*

[e]*University of Chinese Academy of Sciences, Beijing 100049, P. R. China*

† Electronic supplementary information (ESI) available. CCDC 2261655, 2261661, 2261656 and 2261662. For ESI and crystallographic data in CIF or other electronic format see DOI: https://doi.org/10.1039/d4sc03642e

‡ These authors contributed equally.

sulfur substitution, it has been observed that such PSs tend to aggregate in aqueous media,[34] and whether and how this aggregation affects the excited state dynamics and $^1O_2$ photosensitization has yet to be investigated.[35–37]

Porpholactones and their derivatives, in which one or two oxazolone moieties replace the pyrrole units in porphyrin, feature intriguing photophysical properties such as chlorophyll-like strong absorption at the near-infrared (NIR) region, and synthetic flexibility arising from the oxazolone moiety.[38–40] Previously, we used Lawesson's reagent to prepare the porphothiolactone that shows a bathochromic shift of Q bands and remarkable fluorescence quenching, suggesting an enhanced ISC rate and narrowed HOMO–LUMO gap.[41,42] In this work, we prepared a series of porphodilactones to investigate the effects of the extent of thiolation and regioisomerism on the molecular packing in crystals and photophysical properties. We then used DSPE-mPEG$_{2000}$ (1,2-distearoyl-*sn*-glycero-3-phosphoethanolamine-*N*-[methoxy(polyethylene glycol)$_{2000}$])[43] to prepare the water-soluble nanoparticles, allowing for the examination of the sulfur substitution-induced aggregation and photophysical properties in aqueous media. Notably, more sulfur substitution can switch off $^1O_2$ photosensitization in aqueous media, in contrast to the expected trend observed in organic solvents. To better understand the excited state dynamics, we conducted transient absorption spectroscopic studies to investigate their excited state dynamics, along with the density functional theory (DFT) calculations and molecular dynamics (MD) simulations. We found that progressive β-thiolation indeed promotes the ISC processes and populating triplets in both CH_2Cl_2 and aqueous media. However, this is not sufficient to interpret the "switched-off" $^1O_2$ photosensitization for more sulfur substitution. We then simulated sulfur substitution-induced aggregation, and importantly, the extent of thiolation significantly affects the energy levels of the aggregate models and $^1O_2$ photosensitization, leading to different energy dissipation pathways (Scheme 1). Finally, we performed the PDT treatment in cells, 3D multicellular spheres, and *in vivo* mice models to demonstrate the photocytotoxicity of porphyrin PSs. Interestingly, lower photocytotoxicity was obtained in living cells and multicellular spheroids for more sulfur-substituted porphyrins, consistent with the switched-off $^1O_2$ photosensitization in aqueous media. Therefore, these findings can provide broader guidance for evaluating innovative PSs from a single molecule and the possible molecular aggregates under physiological conditions, which may occur in preclinical and clinical studies for actual PDT treatments.

Results and discussion

Synthesis, characterization, and photophysical properties

Lawesson's reagent is a classic thiolation agent that can replace oxygen atoms in the carbonyl group with sulfur atoms.[44] *meso*-C_6F_5-substituted porphodilactones (a mixture of *cis*- and *trans*-isomers) were mixed with Lawesson's reagent (20 equiv.) in toluene under reflux for 3 days to afford *cis*/*trans*-porphothiodilactone isomers with moderate yields of 20 and 15%, respectively (Fig. 1a). In a one-pot synthesis, the products with different extents of thiolation and different orientations of β-substituents (termed ***cis*-O'S**, ***cis*-S'S**, ***trans*-O'S**, and ***trans*-S'S**) at the opposite pyrrole positions could be isolated by silica gel chromatography. These new compounds were fully characterized by ^1H and ^{19}F NMR (nuclear magnetic resonance spectroscopy, Fig. S1–S4†), HR-MS (high-resolution mass spectrometry, Fig. S5†), and FT-IR (Fourier transform infrared spectroscopy, Fig. S6†). Single crystals of ***cis*-O'S** (CCDC: 2261655), ***cis*-S'S** (CCDC: 2261661), ***trans*-O'S** (CCDC: 2261656), and ***trans*-S'S** (CCDC: 2261662) were obtained by diffusing methanol into $CHCl_3$ solution, respectively. Table S1†

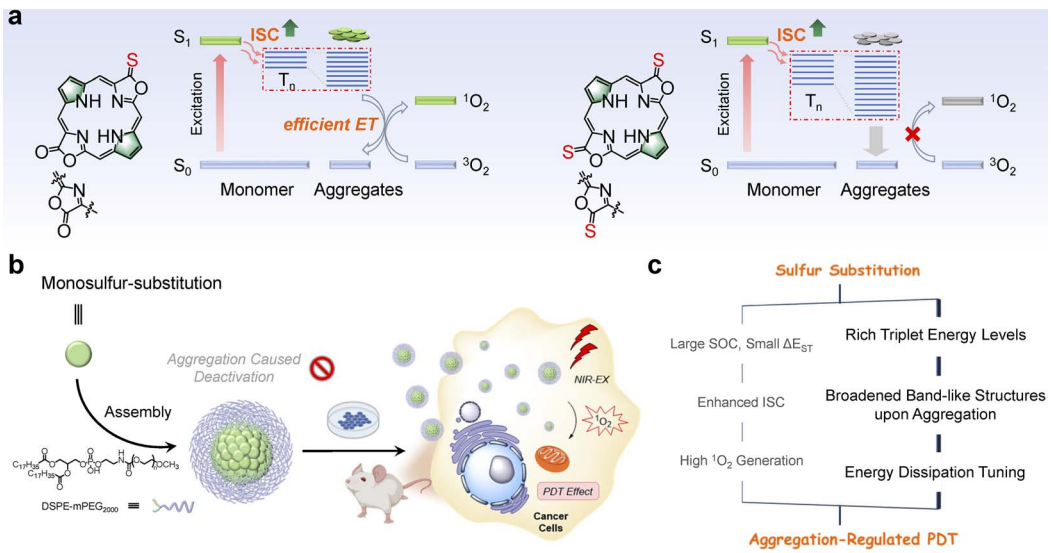

Scheme 1 (a) Molecular structure of ***cis*-O'S** and ***cis*-S'S** and the excited state energy dissipation pathways in their aggregated states. (b) Schematic illustration of the ***cis*-O'S** self-assembly into nanospheres and subsequent PDT effect. (c) The proposed sulfur substitution strategy to obtain aggregation-regulated PDT effect by tuning excited state dynamics.

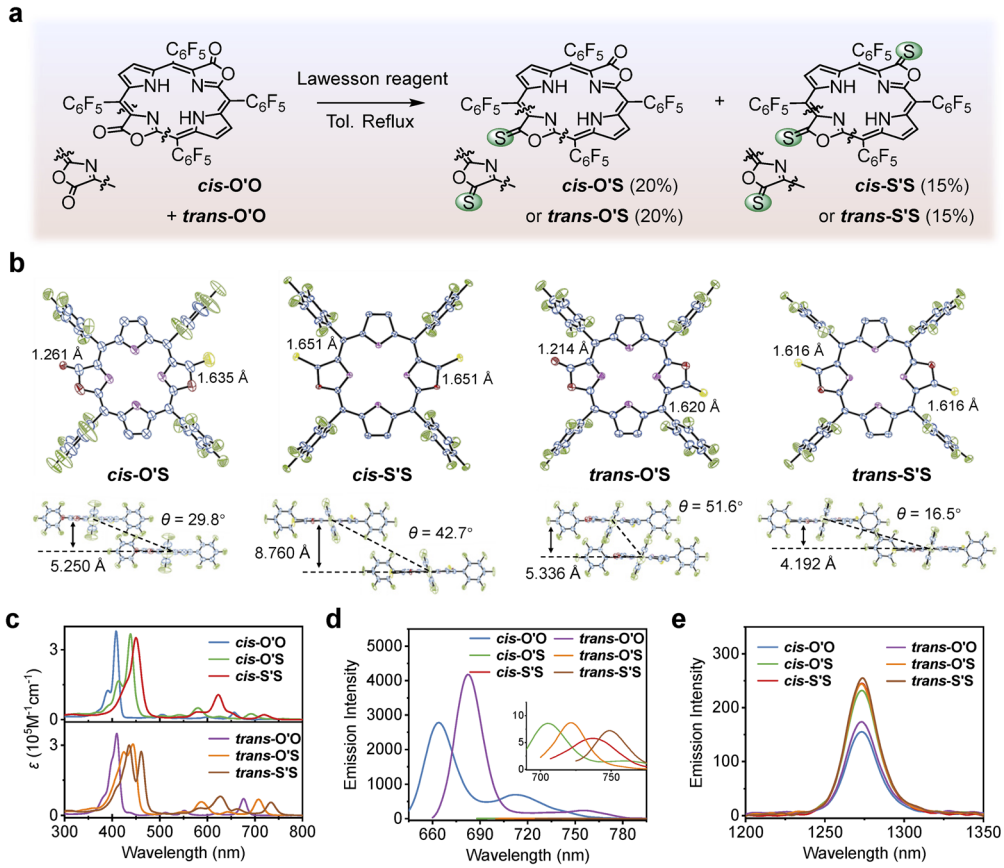

Fig. 1 (a) One-pot synthesis of porphothiodilactone isomers. (b) X-ray crystal structures of *cis*-/*trans*-O'S, and *cis*-/*trans*-S'S. Hydrogen atoms and solvents are omitted for clarity. (c) Absorption spectra of *cis*-/*trans*-O'O, *cis*-/*trans*-O'S, and *cis*-/*trans*-S'S in CH_2Cl_2. (d) Emission spectra of *cis*-/*trans*-O'O, *cis*-/*trans*-O'S, and *cis*-/*trans*-S'S in CH_2Cl_2 with excitation at 405 nm ($A_{405} = 0.10$). (e) Phosphorescence spectra of $^1O_2$ obtained from air-saturated CH_2Cl_2 solutions of *cis*-/*trans*-O'O, *cis*-/*trans*-O'S, and *cis*-/*trans*-S'S.

summarizes crystal structure data collection and refinement statistics. Fig. 1b shows the differing arrangements of lactone moieties in *cis*- and *trans*-porphothiodilactones. The bond length of C=S in porphothiodilactones is approximately 1.616–1.651 Å, which is close to the C=S bond length (1.665 Å) in porphothiolactone,[42] but longer than that of C=O bonds (1.214–1.261 Å) due to the smaller electronegativity of S.

The introduction of sulfur atoms causes local distortion of the N_4 macrocycle and affects the intermolecular packing modes. ***Cis***- and ***trans*-O'S** crystallize in monoclinic cells with $P2_1/c$ and $P2_1/n$ space groups, respectively. Meanwhile, ***cis***- and ***trans*-S'S** crystallize in tetragonal cells ($I4/m$ space group) and orthorhombic cells (*Pbca* space group), respectively (Fig. S7†). ***Cis*-O'S** adopts mixed packing modes with two different orientations with a dihedral angle (φ) of 51.5°. The vertical distance between two π-stacked molecules is 5.250 Å with a slip angle (θ) of 29.8°. ***Cis*-S'S** is arranged in an edge-to-face manner (φ = 90.0°) with a distance of 3.065 Å between S atom and π plane and a vertical distance of 8.760 Å between two parallel molecules with a slip angle (θ) of 42.7°. The two packing modes in ***trans*-O'S** are also almost perpendicular (φ = 84.2°), and the distance between two π-stacked molecules is 5.336 Å (θ = 51.6°). There are four orientations of packing in the cell of ***trans*-S'S** (φ = 28.3°, 56.5°, 64.8°), and the distance between two π-stacked molecules is 4.192 Å (θ = 16.5°). Overall, the slip angles of π-stacked molecules are less than 54.7°, indicating *J*-aggregation.[45] Besides, monosulfur substitution (***cis***- and ***trans*-O'S**) leads to a relatively loose packing (ρ = 1.535 or 1.645 g cm^{-3}), and disulfur substitution (***cis***- and ***trans*-S'S**) leads to a relatively tight packing (ρ = 1.652 or 1.729 g cm^{-3}) with more molecules and smaller spacing in cells. These results show that the replacement of O with S atoms influences the crystal structure and the aggregation of molecules.

The UV-vis absorption and emission spectra of *cis*/*trans*-porphothiodilactone derivatives were recorded in CH_2Cl_2 at room temperature (Fig. 1c and d). Photophysical data from this study are summarized in Table S2.† β-Thiolation of porphodilactones resulted in a significant red-shift of Soret bands compared to porphodilactones without S substitution. As the extent of thiolation increased, a stepwise red-shift in the lower energy Q band was observed. For *cis*-isomers, it started from 656 nm (***cis*-O'O**), then shifted to 692 nm (***cis*-O'S**), and finally reached 720 nm (***cis*-S'S**). For *trans*-isomers, S substitution leads to a red-shift in Q bands, from 676 nm (***trans*-O'O**) to 708 nm (***trans*-O'S**) and 734 nm (***trans*-S'S**), respectively. The cyclic voltammograms (CVs) showed a progressive decrease in HOMO–

LUMO gap values as the extent of thiolation increased (1.89 eV for ***cis*-O'O**, 1.74 eV for ***cis*-O'S**, 1.58 eV for ***cis*-S'S**; 1.78 eV for ***trans*-O'O**, 1.59 eV for ***trans*-O'S**, 1.47 eV for ***trans*-S'S**, Table S3†). This suggested that S substitution is an effective strategy for remodeling energy levels of the frontier molecular orbitals and inducing NIR absorption (Fig. S8†).[46,47]

Regarding fluorescence, ***cis*-/*trans*-O'S** and ***cis*-/*trans*-S'S**, demonstrate weak fluorescence with minimal quantum yields (Φ_{em}s < 0.1%), in contrast to the strong emission of porphodilactones (***cis*-/*trans*-O'O**) in CH_2Cl_2 (Φ_{em}s ~15%).[48] Then, we measured the $^1O_2$ characteristic emission at *ca.* 1275 nm in air-saturated CH_2Cl_2 solution, as depicted in Fig. 1e. On measuring the $^1O_2$ characteristic emission at *ca.* 1275 nm in air-saturated CH_2Cl_2 solution, the $^1O_2$ quantum yields (Φ_Δs) of 79–82% were measured (Table S2†) upon photoexcitation of ***cis*-/*trans*-O'S** and ***cis*-/*trans*-S'S**, much higher than those obtained by porphodilactones (***cis*-/*trans*-O'O**, Φ_Δ = 53–60%).[41] Thus, the quenched fluorescence accompanied by the enhanced ability to $^1O_2$ photosensitization demonstrates that β-thiolation enhances the ISC process.[49] Additionally, regarding $^1O_2$ generation, a further increase of sulfur substitution from 1 to 2 and the relative orientation of β-substituents have trivial effects.

Photophysical properties in aqueous media

To explore the phototherapeutic potential of porphothiodilactones, ***cis*-/*trans*-O'O**, ***cis*-/*trans*-O'S**, and ***cis*-/*trans*-S'S** were prepared into nanoparticle (NP) formulations (***cis*-O'O@NPs**, ***cis*-O'S@NPs**, ***cis*-S'S@NPs**, ***trans*-O'O@NPs**, ***trans*-O'S@NPs**, and ***trans*-S'S@NPs**) using DSPE-mPEG$_{2000}$ as the biocompatible matrix (Fig. 2a). Transmission electron microscopy images show that there are spherical NPs present with diameters of approximately 10 nm (Fig. S9†), regardless of S substitutions or isomerization. Dynamic light scattering (DLS) analysis of porphothiodilactone NPs in water shows the average particle sizes with hydrodynamic diameters of *ca.* 13 nm (Fig. S10†).

Then, the aggregation behaviors of PSs inside NPs were analyzed according to their absorption in water. As shown in Fig. 2b and S11,† ***cis*-O'O@NPs**, and ***cis*-O'S@NPs** exhibited broadened absorption without an apparent band shift, whereas ***cis*-S'S@NPs** showed clear red-shifted Q-bands (from 550 to 800 nm) compared to the molecular form. Such a shift is a characteristic absorption due to *J*-aggregation, leading to lower energy. Similarly, in the case of *trans*-isomers, ***trans*-O'O@NPs**, and ***trans*-O'S@NPs** demonstrated blue-shifted Q-bands or Q-band splitting in the 600–700 nm region, indicating the formation of *H*-aggregates. Interestingly, ***trans*-S'S@NPs**, just like ***cis*-S'S@NPs**, showed red-shifted Q-bands in nanoparticles. Thus, we found that, along with the increase in the extent of β-thiolation, porphothiodilactones may tend to form *J*-aggregates inside NPs.[50]

The trend of porphothiodilactone aggregation was also confirmed by the shifts of their characteristic absorption bands in tetrahydrofuran (THF)/water mixtures with varying ratios (v/v), as shown in Fig. S12.† As the water fraction increases, the absorption spectra of porphothiodilactones gradually align with those of nanoparticles. Additionally, the particles formed in water are significantly larger (hydrodynamic diameters of 160–350 nm) than those coated with DSPE-mPEG$_{2000}$ (Fig. S13†), indicating that porphothiodilactones can aggregate without PEG protection. These results suggest that the encapsulation

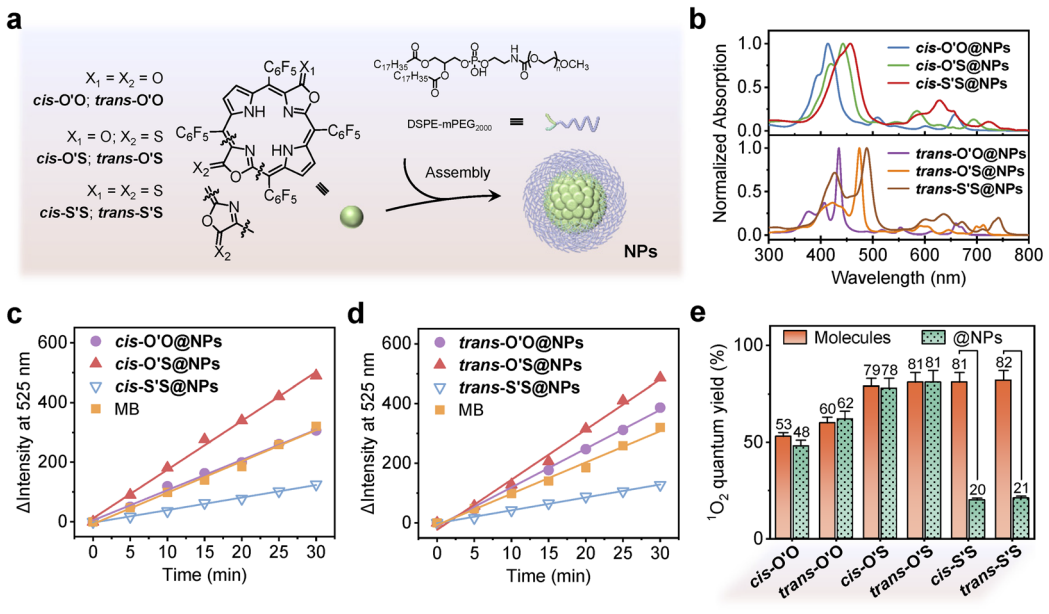

Fig. 2 (a) Preparation of porphodilactone nanoparticles. (b) Absorption spectra of ***cis*-O'O@NPs**, ***cis*-O'S@NPs**, ***cis*-S'S@NPs**, ***trans*-O'O@NPs**, ***trans*-O'S@NPs**, and ***trans*-S'S@NPs** in aqueous solution. (c) Variation of SOSG emission intensity at 525 nm (λ_{ex} = 488 nm) under light irradiation (700 nm, 5 mW cm^{-2}, 0–30 min) in the presence of ***cis*-O'O@NPs**, ***cis*-O'S@NPs**, ***cis*-S'S@NPs**, and MB. (d) Variation of SOSG emission intensity at 525 nm (λ_{ex} = 488 nm) under light irradiation (700 nm, 5 mW cm^{-2}, 0–30 min) in the presence of ***trans*-O'O@NPs**, ***trans*-O'S@NPs**, ***trans*-S'S@NPs**, and MB. (e) Comparison of $^1O_2$ quantum yields between porphodilactone molecules and nanoparticles.

using the amphiphilic phospholipid polymer promotes and stabilizes the aggregation of the photosensitizers in small sizes.

Porphothiodilactone NPs as $^1O_2$ photosensitizers were evaluated by employing the commercially available singlet oxygen sensor green (SOSG) as an indicator (Fig. 2c and d). Upon irradiation with the laser (700 nm, 5 mW cm^{-2}), the strong emission of SOSG at 525 nm appeared in the presence of ***cis*-O'O@NPs**, ***trans*-O'O@NPs**, ***cis*-O'S@NPs**, or ***trans*-O'S@NPs**, indicating their remarkable capability towards $^1O_2$ production (Fig. S14†). As expected, by using methylene blue (MB) as a reference, the $^1O_2$ quantum yields of *ca.* 80% for ***cis*-O'S@NPs** and ***trans*-O'S@NPs** were obtained (Fig. 2e and Table S4†), much higher than those of ***cis*-O'O@NPs** (48%) and ***trans*-O'O@NPs** (62%).

However, the irradiation of ***cis*-S'S@NPs** or ***trans*-S'S@NPs** led to small spectral changes of SOSG with sharply declined $^1O_2$ quantum yields of *ca.* 20%, suggesting much lower efficiency in sensitizing O_2 compared to those in CH_2Cl_2 solution. It is worth noting that long-time (30 min) irradiation (700 nm, 5 mW cm^{-2}) of all porphothiodilactone NPs does not lead to apparent changes in absorption (<5%, Fig. S15†), ruling out photostability as a cause of lower $^1O_2$ photosensitization. Based on morphological studies and absorption in aqueous solution, we assumed that aggregation of PSs inside DSPE nanoparticles plays a critical role in tuning the excited states and, in turn, reacting with O_2.

The photothermal effects of ***cis*-O'S@NPs**, ***cis*-S'S@NPs**, ***trans*-O'S@NPs**, and ***trans*-S'S@NPs** were investigated under laser irradiation (700 nm, 1 W cm^{-2}). The temperature increased by *ca.* 15 °C, with the photothermal conversion efficiencies (η) being 18–26% (Fig. S16 and Table S4†), indicating the modest photothermal performance of porphothiodilactone NPs.

Excited state dynamics

To investigate the dynamics of triplet states for porphodilactone derivatives, we utilized nanosecond (ns) transient absorption (TA) spectroscopy in CH_2Cl_2. Our focus was on *cis*-isomers, as the regioisomerism has a negligible effect on the aggregation of these compounds. After photoexcitation at 355 nm, we observed excited state absorption (ESA) bands in the 450–650 nm spectral range which are attributed to $T_1 \rightarrow T_n$ transitions in ***cis*-O'O**, along with ground state bleaching (GSB) centered at 405 and 652 nm (Fig. S17†). Notably, ns-TAs of ***cis*-O'S** and ***cis*-S'S** showed more ESA bands within the wavelength range of 450–700 nm. Furthermore, we determined the decay rates of the triplet states under degassed conditions to be 11 μs for ***cis*-O'S** and ***cis*-S'S**, representing a significant decrease compared to ***cis*-O'O** porphodilactone (39 μs, Fig. S18†).

We then conducted femtosecond (fs) transient absorption studies to compare the excited state dynamics of ***cis*-O'O**, ***cis*-O'S**, ***cis*-S'S** in CH_2Cl_2 and ***cis*-O'O@NPs**, ***cis*-O'S@NPs**, ***cis*-S'S@NPs** in water. As shown in Fig. 3a, for ***cis*-O'O** in CH_2Cl_2 and ***cis*-O'O@NPs** in water, the initial TA spectra probe at 0.5 ps showed identical features as observed by excited state absorption (ESA, 500–650 nm) and ground state bleaching (GSB, 650–800 nm), indicating that the absorption feature stems from the localized excited (^{1}LE) state. The fs-TA spectra decayed in nanoseconds, corresponding to the fluorescence of ***cis*-O'O** in CH_2Cl_2 and nonradiative relaxation process of ***cis*-O'O@NPs** in water,[51] respectively, and the long-lived state was identified as the triplet state (^{3}LE) by ns-TA spectroscopy.

For ***cis*-O'S** in CH_2Cl_2 and ***cis*-O'S@NPs** in water, the initial TA spectra (~0.3 ps) also feature the ^{1}LE character, where a major ESA band and a major GSB band probe were centered at 650 and 700 nm, respectively. Within a few seconds (<2 ps), the singlet state efficiently forms, and the ISC process from the singlet to triplet states dominates during a period of 2–200 ps, accompanied by a pronounced increase centered on 650 nm in the ESA (Fig. 3b). A global analysis of the TA spectra unambiguously reveals that excited states under different conditions share similar properties, as indicated by the corresponding kinetic rate constants (k) of 3.7×10^{10} s^{-1} and 3.4×10^{10} s^{-1} obtained for ***cis*-O'S** in CH_2Cl_2 and ***cis*-O'S@NPs** in water (Table S5†), respectively. Over the following 200–3600 ps, the ESA and GSB bands exhibit slow decay to the ground state, consistent with the long lifetime obtained in ns-TA spectroscopy. Similarly, ***cis*-S'S** in CH_2Cl_2 and ***cis*-S'S@NP**s in water exhibited comparable kinetics in the excited states ($k = 3.9 \times 10^{10}$ s^{-1} and 4.1×10^{10} s^{-1}, respectively), as shown in Fig. 3c. During 200–3600 ps, the features of ESA and GSB of photoexcited ***cis*-S'S** in CH_2Cl_2 exhibit a much faster decay ($k = 1.8 \times 10^8$ s^{-1}) towards the ground state than that seen in ***cis*-S'S@NPs** in water (unable to fit, Table S5†), probably due to slower relaxation of triplet states arising from aggregation of PSs in NPs.

Replacing S atom leads to a clear ISC process from the S_1 to the T_1 state, which is not present for ***cis*-O'O** in CH_2Cl_2 or water, making triplet generation more efficient. While increasing the S atom replacement from 1 to 2 does not significantly enhance the triplet state population, it does extend the lifetime in the nanoparticle form. We assume that the tendency for aggregation, as seen in the absorption and crystalline structure, is responsible for slowing the relaxation of triplet states. Interestingly, both ***cis*-O'S@NPs** and ***cis*-S'S@NPs** in water efficiently populate triplet states when exposed to light; however, only ***cis*-O'S@NPs** can effectively photosensitize $^1O_2$ in a high quantum yield. Therefore, more than the current studies on excited state dynamics may be required to fully understand the deactivation of $^1O_2$ production in ***cis*-S'S@NPs** in water.

Theoretical and computational studies

To gain insights into the triplet states of ***cis*-O'S** and ***cis*-S'S** isomers and their aggregates, we performed time-dependent density functional theory (TD-DFT) calculations to optimize the structures of porphodilactones and porphothiodilactones based on their crystal structures.[52] We observed the impact of sulfur substitution on excited state features for *cis*- and *trans*-isomers, and SOC constants after thiolation exhibit a significant increase (Tables S6 and S7,† *e.g.* 1.10 cm^{-1} for ***cis*-O'O**, 11.9 cm^{-1} for ***cis*-O'S**, and 37.1 cm^{-1} for ***cis*-S'S**). The enhancement of SOC promotes the ISC process with increasing rate constants (k_{ISC}) from 5.03×10^6 s^{-1} for ***cis*-O'S**, to 4.63×10^8 s^{-1}

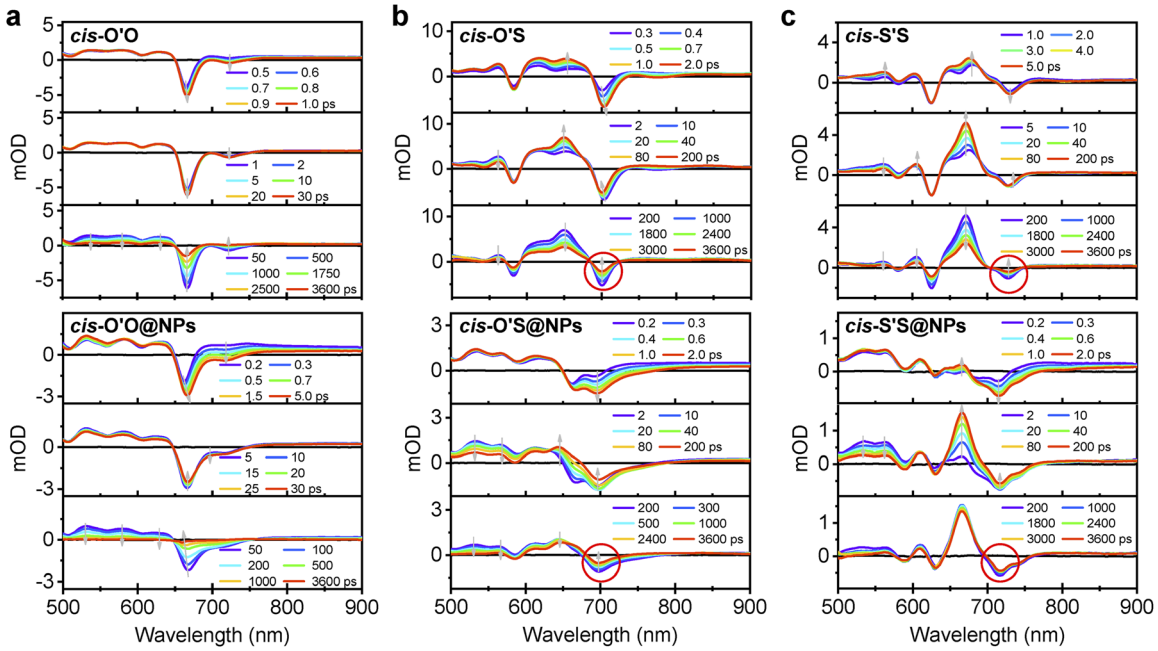

Fig. 3 (a) Femtosecond transient absorption (fs-TA) difference spectra for ***cis*-O'O** recorded in CH_2Cl_2 (0.5–1 ps, 1–30 ps, and 50–3600 ps) and ***cis*-O'O@NPs** recorded in H_2O (0.2–5 ps, 5–30 ps, and 50–3600 ps) monitored over different delay regimes. (b) Femtosecond transient absorption (fs-TA) difference spectra for ***cis*-O'S** recorded in CH_2Cl_2 (0.3–2 ps, 2–200 ps, and 200–3600 ps) and ***cis*-O'S@NPs** recorded in H_2O (0.2–2 ps, 2–200 ps, and 200–3600 ps) monitored over different delay regimes. (c) Femtosecond transient absorption (fs-TA) difference spectra for ***cis*-S'S** recorded in CH_2Cl_2 (1–5 ps, 5–200 ps, and 200–3600 ps) and ***cis*-S'S@NPs** recorded in H_2O (0.2–2 ps, 2–200 ps, and 200–3600 ps) monitored over different delay regimes.

and 8.75×10^8 s^{-1} for ***cis*-O'S** and ***cis*-S'S**, respectively. These calculated results are consistent with the experimental observation of fluorescence quenching and the enhanced $^1O_2$ production after sulfur atom replacement of porphodilactones. Notably, sulfur atom replacement stabilizes the LUMO level and destabilizes the HOMO, thus reducing the energy gap and shifting the absorption to a long wavelength. This also leads to a strong lowering of the energies of the triplet states, resulting in the emergence of new ISC channels between the singlet and triplet excited states, as illustrated in Fig. S19–S20.† Importantly, this highlights the crucial role of sulfur substitution in promoting the population of the triplet states.

To further investigate the effect of aggregation inside NPs on the population of triplet states, a molecular dynamics (MD) simulation was performed which provided insights into the distribution of conformational structures with short-range (<10 Å) ordering over a span of 200 ns.[53,54] As illustrated in Fig. 4a, the molecules confined within a water box ($50 \times 50 \times 50$ Å) exhibit an aggregation tendency due to hydrophobicity and π–π interaction, resulting in distinct dimer and trimer structures with an inclination observed within the clusters. Remarkably, the ***cis*-S'S** molecules adopt nearly parallel conformations, featuring a dihedral angle of approximately 10.5° and an intermolecular distance of approximately 4.81 Å between the π-stacked dimers. The distribution of transition dipole moments within ***cis*-S'S** dimers follows a normal distribution, indicative of the simulation having reached the thermodynamic steady state. The obtained average angle of 19.2° (<54.7°) provides additional evidence for the propensity of ***cis*-S'S** to form *J*-aggregates at higher concentrations (Fig. 4b). In contrast, ***cis*-O'O** and ***cis*-O'S** display non-parallel aggregation patterns, characterized by dihedral angles of approximately 60° (Fig. S21†). Additionally, specific ***trans*-O'O** molecules display *H*-aggregation characteristics with a dihedral angle of less than 15° and a transition dipole moment angle larger than 54.7° (Fig. S22†).[51] The simulation outcomes underscore the distinct aggregation tendency of porphodilactones within NPs, where monosulfur-substituted NPs are filled with mixed packing modes. In contrast, disulfur-substituted ones form a stable *J*-aggregation,[55] consistent with UV-vis absorption in Fig. 2 and S11.†

To further elucidate the impact of aggregation on the PDT effect, we chose the dimer structures of ***cis*-O'O**, ***cis*-O'S**, and ***cis*-S'S** obtained by MD simulations. We then calculated the energy levels of singlet and triplet states (as shown in Fig. 4c). As shown in Fig. S23–S25,† these dimers exhibit more energy levels of triplet states below the S_1 state than monomeric molecules. This is due to the π–π interactions and excitonic coupling among adjacent molecules in aggregation that cause the splitting of excited energy levels as per Kasha's rules.[56] The formation of band-like structures can potentially introduce multiple pathways for deactivating triplets in porphothiodilactones.[57]

Specifically, we found that in the case of ***cis*-S'S-dimer**, the energy levels of the triplet state are inherently lower than that of $^1O_2$ (1270 nm, $^1\Delta_g \rightarrow {}^3\Sigma_g$ transition). In contrast, weak π–π interaction in non-parallel aggregation causes the energy levels for the triplet states of ***cis*-O'S-dimer** to remain higher than $^1O_2$,

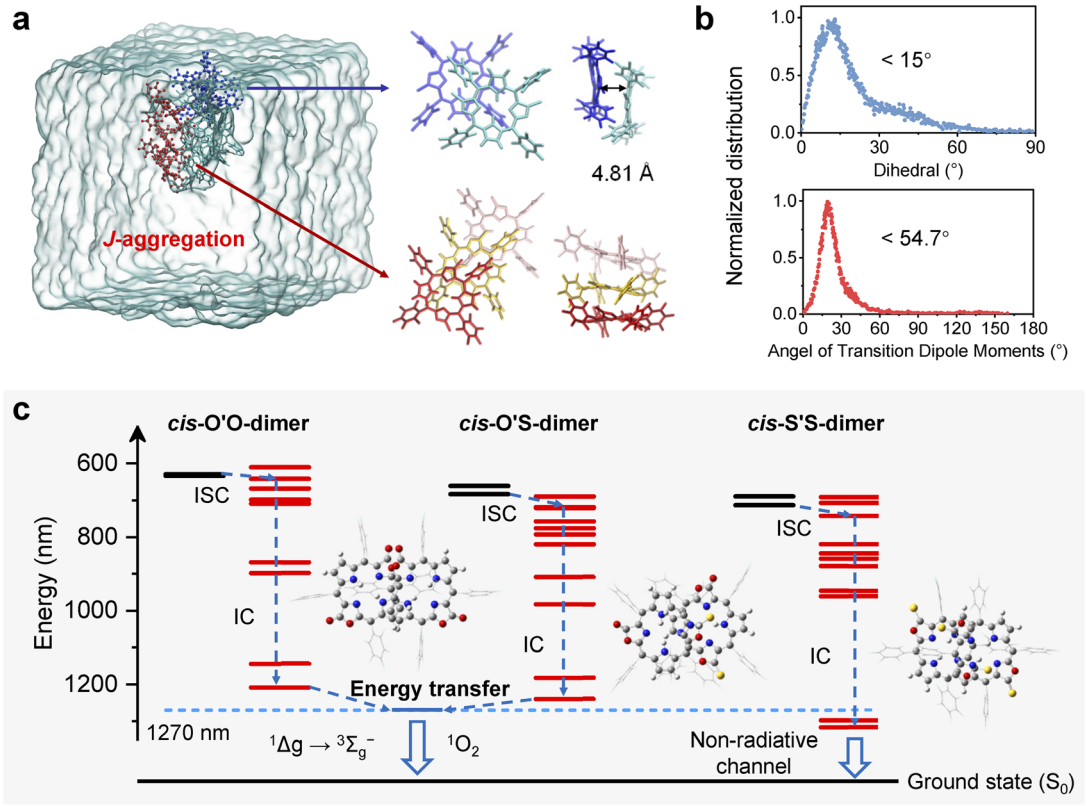

Fig. 4 (a) Schematic illustration of the molecular aggregation of ***cis*-S'S** expected to persist in nanoparticles as deduced from equilibrated MD simulations in a water box (50 × 50 × 50 Å) and expected arrangements of the constituent aggregated dimers and trimers. (b) Normalized distribution of dihedral and transition dipole moment angle between ***cis*-S'S** dimers. (c) Depiction of the proposed excited state energy dissipation pathways and triplet energy levels of ***cis*-O'O**, ***cis*-O'S**, and ***cis*-S'S** dimers.

promoting efficient intermolecular energy transfer and ultimately leading to $^1O_2$ generation. This attenuation of $^1O_2$ generation in ***cis*-S'S** NPs is particularly pronounced. On the other hand, the larger SOC parameter between T_1 and S_0 for ***cis*-S'S-dimer** (4.38 cm^{-1}) was present, in comparison to ***cis*-O'O-dimer** (0.73 cm^{-1}) and ***cis*-O'S-dimer** (3.02 cm^{-1}). These results highlight different energy dissipation pathways observed between monosulfur- and disulfur-substituted porphodilactones inside NPs in water, which can be attributed to progressive β-thiolation that leads to porphyrinoid aggregation.

In vitro and *in vivo* experiments

To explore the impact of thiolation on $^1O_2$ photosensitization of ***cis*-O'S@NPs** and ***cis*-S'S@NPs** in living cells, we used 2′,7′-dichlorofluorescein diacetate (DCFH-DA) as a probe to measure intracellular ROS levels. In Fig. 5a, we observed bright green fluorescence in HeLa cells after exposure to ***cis*-O'S@NPs** upon photoirradiation (700 nm, 10 mW cm^{-2}, 10 min) in contrast to weak intracellular fluorescence in cells treated with ***cis*-S'S@NPs** + *hν*. This is consistent with the low efficiency of $^1O_2$ generation of ***cis*-S'S@NPs** in water. Under dark conditions, there was trivial ROS generation when cells were treated with ***cis*-O'S@NPs** or ***cis*-S'S@NPs**.

Next, we assessed the photocytotoxicity of ***cis*-O'S@NPs** and ***cis*-S'S@NPs** on HeLa cells using a Cell Counting Kit-8 (CCK-8). After irradiation at 700 nm (10 mW cm^{-2}) for 10 min, ***cis*-O'S@NPs** showed dose-dependent cytotoxicity with a low half-maximal inhibitory concentration (IC_{50}) of 0.50 μM (Fig. 5b), whereas ***cis*-S'S@NPs** exhibited weak photocytotoxicity with an IC_{50} of 13.7 μM. There was no significant dark cytotoxicity observed for either ***cis*-O'S@NPs** or ***cis*-S'S@NPs** as cell viability remained above 80% even at a concentration of 10 μM (Fig. S26†). We also used calcein-AM and propidium iodide (PI) to identify live (green) and dead (red) cells (Fig. 5c). The results showed a high level of cell death with red fluorescence in cells treated with ***cis*-O'S@NPs** and subjected to photoirradiation, whereas a portion of cells remained alive in ***cis*-S'S@NPs** + *hν*.

To evaluate their effectiveness on multicellular spheroids (MCSs), we conducted PDT experiments using ***cis*-O'S@NPs** or ***cis*-S'S@NPs**. MCSs are commonly used to simulate solid tumor microenvironments.[58] After incubation with ***cis*-O'S@NPs** or ***cis*-S'S@NPs**, the MCSs were then divided into dark and light groups and exposed to photoirradiation (700 nm, 10 mW cm^{-2}, 10 min).

As shown in Fig. 5e, the results showed that treatment with ***cis*-O'S@NPs** or ***cis*-S'S@NPs** significantly inhibited the growth of MCSs, while the control groups under dark incubation dramatically increased in volume after seven days (Fig. S27†). Additionally, the morphology of MCSs in the light groups changed significantly. On day 6, the MCSs treated with ***cis*-**

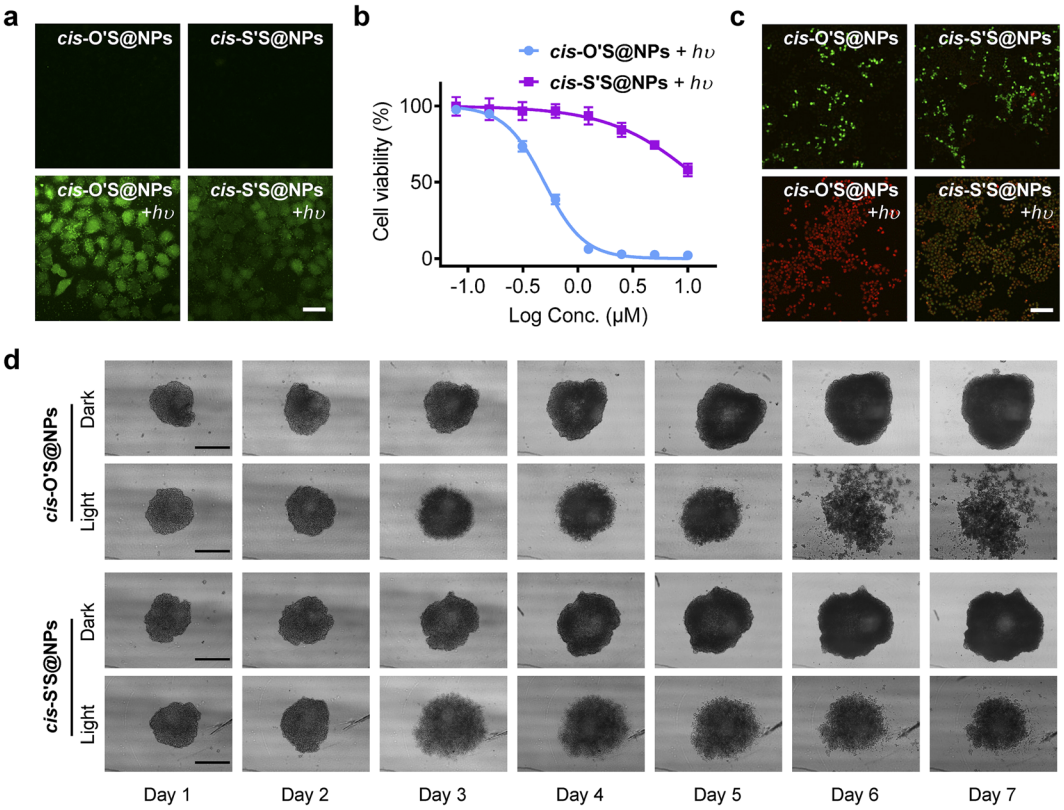

Fig. 5 (a) Intracellular ROS level of HeLa cells treated with ***cis*-O'S@NPs** and ***cis*-S'S@NPs** under dark and light conditions (700 nm, 10 mW cm^{-2}, 10 min), respectively. DCFH-DA was used as the fluorescent probe for ROS generation. Scale bar: 50 μm. (b) Photocytotoxicity of ***cis*-O'S@NPs** and ***cis*-S'S@NPs** (0–10 μM) on HeLa cells obtained by a CCK-8 assay. (c) Fluorescence images of Calcein AM/PI-stained HeLa cells treated with ***cis*-O'S@NPs** and ***cis*-S'S@NPs** under dark and light conditions, respectively. Scale bar: 200 μm. (d) Images of HeLa 3D MCSs treated with ***cis*-O'S@NPs** and ***cis*-S'S@NPs** (6 μM) under dark and light conditions, respectively. The images for day 1 were recorded before irradiation. Scale bar: 500 μm.

O'S@NPs + *hυ* showed a remarkable collapse, indicating that ***cis*-O'S@NPs** had a higher PDT efficacy than ***cis*-S'S@NPs** under the same conditions. These findings suggest that the extent of β-thiolation effectively influences $^1O_2$ photosensitization in living cells and MCSs.

We then extended our study to a mouse model (Fig. 6a). The mice were randomly divided into five groups: "control (PBS + *hυ*)", "***cis*-O'S@NPs**", "***cis*-S'S@NPs**", "***cis*-O'S@NPs** + *hυ*", and "***cis*-S'S@NPs** + *hυ*" with each group consisting of four mice. After 24 hours of tail vein injection, we irradiated the tumor sites using a 700 nm LED light for 10 min (200 mW cm^{-2}). We monitored the tumor volumes and mice body weights every two days and analyzed photographs of dissected tumor tissues and tumor weights (Fig. 6b–d). A negligible difference in body weights in all groups was seen (Fig. 6e). We found that both "***cis*-O'S@NPs** + *hυ*" and "***cis*-S'S@NPs** + *hυ*" treatments resulted in a high inhibition of tumor growth (87.0% and 88.6%, respectively). This was in contrast to the control and dark-treated groups, which showed a distinct increase in tumor volume after 14 days of observation. TUNEL staining further confirmed the presence of apoptotic cells in the tumor tissues treated with both "***cis*-O'S@NPs** + *hυ*" and "***cis*-S'S@NPs** + *hυ*" (Fig. S28†). Furthermore, we conducted hematoxylin and eosin (H&E) staining on key organs but observed no destructive cell necrosis or inflammation lesions in any of the groups (Fig. S29†). Our study suggests that replacing the sulfur atom is an effective approach to enhance PDT treatment *in vivo*. However, we did not observe any significant difference in therapeutic effect between ***cis*-O'S@NPs** and ***cis*-S'S@NPs**. As the "switch-on/off" $^1O_2$ photosensitization of ***cis*-S'S** is highly dependent on the molecular aggregation, we hypothesized that the possibility of nanoparticle dissociation and deaggregation of ***cis*-O'S** or ***cis*-S'S** in the tumor microenvironment or during circulation[59,60] led to the recovery of PDT efficacy for monomeric ***cis*-S'S**.

Considering the weak acidity of the tumor microenvironment (TME), we first examined the stability of porphothiodilactone nanoparticles (NPs) in a mildly acidic setting (pH ~ 5.5). When the NPs were placed in a buffer solution with a pH of 5.5 for 24 h, their size increased significantly and exhibited a broad size distribution (Fig. S30†). Additionally, although the efficiency of photothermal conversion for the porphothiodilactone NPs is still low, we observed a thermal effect when we irradiated the tumor sites in mice. After 10 min of irradiation (700 nm, 200 mW cm^{-2}), the temperature of the tumor areas injected with NPs increased by approximately 2 °C (Fig. S31†). This temperature elevation may induce the dissociation of the NPs, as

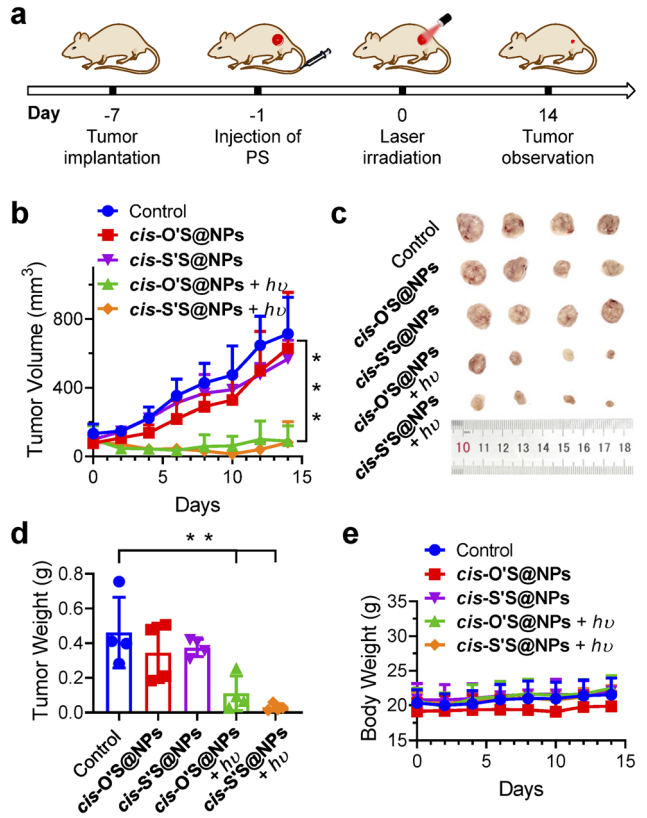

Fig. 6 (a) Schematic illustration of the treatment regimen. (b) Tumor volume variation curves for the mice in control (PBS + $h\upsilon$), *cis*-O'S@NPs, *cis*-S'S@NPs, *cis*-O'S@NPs + $h\upsilon$, and *cis*-S'S@NPs + $h\upsilon$ groups during the treatment period ($n = 4$). ***$p < 0.05$. (c) Digital photographs of the tumors dissected from the mice in different groups. (d) Tumor weight of the mice in different groups at the end of treatment (mean ± SD, $n = 4$, **$P < 0.05$). (e) Body weight curves of the mice in different treatment groups ($n = 4$, mean ± SD).

supported by the photothermal heating curve in solutions and the increased particle size after irradiation (Fig. S32†). Nevertheless, the TME is quite complex and the response mechanisms of specific factors or targets still remains unclear, which needs more effort to understand the possible mechanism and develop switchable photosensitive systems related to aggregation and excited states in our future study.

Conclusions

In summary, we synthesized a range of porphothiodilactone derivatives to investigate the impact of β-thiolation on the photophysical properties and $^1O_2$ photosensitization of porphyrinoids. By replacing oxygen with sulfur atoms at opposite pyrrole positions on the porphyrin periphery, we observed gradual redshifts in absorption and severely quenching emission. Our experiments, including transient absorption spectroscopy, showed that the different sulfur substitutions yielded similar excited state dynamics, promoting the ISC process and improving the population of triplet states. As a result, sulfur substitution effectively increased the $^1O_2$ generation of porphyrinoids. Interestingly, we noted that mono- and disulfur substituted porphyrinoids had different $^1O_2$ photosensitization in various media. This surprising discovery contradicts the traditional "more is better" approach and warrants further exploration.

Through crystal structure analysis, characteristic absorption of *J*-aggregation, and MD simulation, we found that progressive thiolation of the β-periphery led to enhanced aggregation from loose to close packing. Furthermore, TD-DFT calculations of porphothiodilactone aggregation suggested that the energy levels of the triplet states of disulfur-substituted porphyrin aggregates are inherently lower than that of $^1O_2$. In comparison, those of monosulfur-substituted congery have higher energy levels. This leads to different energy dissipation pathways at the excited states between mono- and disulfur-substituted porphodilactone aggregates, which may explain the switching of $^1O_2$ photosensitization in aqueous media. Overall, our work challenges conventional wisdom and offers new insights into understanding the action mechanism of heteroatom-incorporated PSs beyond the molecule level.

Data availability

The data that support the findings of this study are available in the ESI† of this article.

Author contributions

Conceptualization: M. Z., H. Z., and J.-L. Z. Data curation: M. Z., H. Z., and J.-L. Z. Investigation: M. Z. and H. Z. Project administration: M. Z., H. Z., and J.-L. Z. Synthesis section: M. Z., M. W., and Y. Yu. Calculation section: Y. Yao. Spectral section: M. Z. and G. R. Animal section: M. Z., H. Z., and R. Z. Writing – original draft: M. Z. and H. Z. Writing – review & editing: M. Z., H. Z., J. Z., X.-J. L., and J.-L. Z. Funding acquisition: J.-L. Z. Supervision: J. Z., M. Z., and J.-L. Z.

Conflicts of interest

There are no conflicts to declare.

Acknowledgements

Financial support from the National Natural Science Foundation of China (21571007, 21621061, 21778002, and 21861162008) and the Chemistry and Chemical Engineering Guangdong Laboratory (1932002) is acknowledged. The measurements of fluorescence spectroscopy were performed at the Analytical Instrumentation Center of Peking University. This work was supported in part by the High-performance Computing Platform of Peking University. L.-J. Guo and W.-C. Xie are gratefully thanked for TEM measurements and biological experiments. All animal procedures were approved by the Institutional Animal Care and Use Committee of Sinoresearch (Beijing) Biotechnology Co., Ltd (protocol number: ZYZC202306011J).

References

1 X. Li, J. F. Lovell, J. Yoon and X. Chen, Clinical development and potential of photothermal and photodynamic therapies for cancer, *Nat. Rev. Clin. Oncol.*, 2020, **17**, 657–674.
2 X. Zhao, J. Liu, J. Fan, H. Chao and X. Peng, Recent progress in photosensitizers for overcoming the challenges of photodynamic therapy: from molecular design to application, *Chem. Soc. Rev.*, 2021, **50**, 4185–4219.
3 T. C. Pham, V. N. Nguyen, Y. Choi, S. Lee and J. Yoon, Recent strategies to develop innovative photosensitizers for enhanced photodynamic therapy, *Chem. Rev.*, 2021, **121**, 13454–13619.
4 W. Fan, P. Huang and X. Chen, Overcoming the Achilles' heel of photodynamic therapy, *Chem. Soc. Rev.*, 2016, **45**, 6488–6519.
5 E. L. Bastos, F. H. Quina and M. S. Baptista, Endogenous photosensitizers in human skin, *Chem. Rev.*, 2023, **123**, 9720–9785.
6 W. Hu, P. N. Prasad and W. Huang, Manipulating the dynamics of dark excited states in organic materials for phototheranostics, *Acc. Chem. Res.*, 2021, **54**, 697–706.
7 J. Chen, Y. Zhu, C. Wu and J. Shi, Nanoplatform-based cascade engineering for cancer therapy, *Chem. Soc. Rev.*, 2020, **49**, 9057–9094.
8 Z. Zhou, J. Song, L. Nie and X. Chen, Reactive oxygen species generating systems meeting challenges of photodynamic cancer therapy, *Chem. Soc. Rev.*, 2016, **45**, 6597–6626.
9 Y. Gui, Y. Wang, D. Wang, Y. Qin, G. Song, D. Yan, B. Z. Tang and D. Wang, Thiophene π-bridge manipulation of NIR-II AIEgens for multimodal tumor phototheranostics, *Angew. Chem., Int. Ed.*, 2024, **63**, e202318609.
10 G. Feng, G. Q. Zhang and D. Ding, Design of superior phototheranostic agents guided by Jablonski diagrams, *Chem. Soc. Rev.*, 2020, **49**, 8179–8234.
11 Q. Yao, J. Fan, S. Long, X. Zhao, H. Li, J. Du, K. Shao and X. Peng, The concept and examples of type-III photosensitizers for cancer photodynamic therapy, *Chem*, 2022, **8**, 197–209.
12 S. Monro, K. L. Colon, H. Yin, J. Roque, P. Konda, S. Gujar, R. P. Thummel, L. Lilge, C. G. Cameron and S. A. McFarland, Transition metal complexes and photodynamic therapy from a tumor-centered approach: challenges, opportunities, and highlights from the development of TLD1433, *Chem. Rev.*, 2019, **119**, 797–828.
13 M. Zhu, H. Zhang, G. Ran, D. N. Mangel, Y. Yao, R. Zhang, J. Tan, W. Zhang, J. Song, J. L. Sessler and J. L. Zhang, Metal Modulation: An easy-to-implement tactic for tuning lanthanide phototheranostics, *J. Am. Chem. Soc.*, 2021, **143**, 7541–7552.
14 M. Liu, Y. Chen, Y. Guo, H. Yuan, T. Cui, S. Yao, S. Jin, H. Fan, C. Wang, R. Xie, W. He and Z. Guo, Golgi apparatus-targeted aggregation-induced emission luminogens for effective cancer photodynamic therapy, *Nat. Commun.*, 2022, **13**, 2179.
15 D. Liu, A. M. El-Zohry, M. Taddei, C. Matt, L. Bussotti, Z. Wang, J. Zhao, O. F. Mohammed, M. Di Donato and S. Weber, Long-lived charge-transfer state induced by spin-orbit charge transfer intersystem crossing (SOCT-ISC) in a compact spiro electron donor/acceptor dyad, *Angew. Chem., Int. Ed.*, 2020, **59**, 11591–11599.
16 H. Gu, W. Liu, W. Sun, J. Du, J. Fan and X. Peng, Single-molecule photosensitizers for NIR-II fluorescence and photoacoustic imaging guided precise anticancer phototherapy, *Chem. Sci.*, 2022, **13**, 9719–9726.
17 H. Cao, B. Fang, J. Liu, Y. Shen, J. Shen, P. Xiang, Q. Zhou, S. C. De Souza, D. Li, Y. Tian, L. Luo, Z. Zhang and X. Tian, Photodynamic therapy directed by three-photon active rigid plane organic photosensitizer, *Adv. Healthcare Mater.*, 2021, **10**, e2001489.
18 Z. Wang, M. Ivanov, Y. Gao, L. Bussotti, P. Foggi, H. Zhang, N. Russo, B. Dick, J. Zhao, M. Di Donato, G. Mazzone, L. Luo and M. Fedin, Spin–orbit charge-transfer intersystem crossing (ISC) in compact electron donor-acceptor dyads: ISC mechanism and application as novel and potent photodynamic therapy reagents, *Chem.–Eur. J.*, 2020, **26**, 1091–1102.
19 P. Xiao, W. Xie, J. Zhang, Q. Wu, Z. Shen, C. Guo, Y. Wu, F. Wang, B. Z. Tang and D. Wang, De novo design of reversibly pH-switchable NIR-II aggregation-induced emission luminogens for efficient phototheranostics of patient-derived tumor xenografts, *J. Am. Chem. Soc.*, 2023, **145**, 334–344.
20 H. Huang, D. Ma, Q. Liu, D. Huang, X. Zhao, Q. Yao, T. Xiong, S. Long, J. Du, J. Fan and X. Peng, Enhancing intersystem crossing by intermolecular dimer-stacking of cyanine as photosensitizer for cancer therapy, *CCS Chem.*, 2022, **4**, 3627–3636.
21 Z. Zhang, W. Xu, M. Kang, H. Wen, H. Guo, P. Zhang, L. Xi, K. Li, L. Wang, D. Wang and B. Z. Tang, An all-round athlete on the track of phototheranostics: subtly regulating the balance between radiative and nonradiative decays for multimodal imaging-guided synergistic therapy, *Adv. Mater.*, 2020, 32.
22 C. Ji, Q. Gao, X. Dong, W. Yin, Z. Gu, Z. Gan, Y. Zhao and M. Yin, A size-reducible nanodrug with an aggregation-enhanced photodynamic effect for deep chemo-photodynamic therapy, *Angew. Chem., Int. Ed.*, 2018, **57**, 11384–11388.
23 Z. Deng, J. Zhang, J. Zhou, W. Shen, Y. Zuo, J. Wang, S. Yang, J. Liu, Y. Chen, C. C. Chen, G. Jia, P. Alam, J. W. Y. Lam and B. Z. Tang, Dynamic transition between monomer and excimer phosphorescence in organic near-infrared phosphorescent crystals, *Adv. Mater.*, 2024, e2311384.
24 Z. Zhuang, J. Li, P. Shen, Z. Zhao and B. Z. Tang, Exploring and leveraging aggregation effects on reactive oxygen species generation in photodynamic therapy, *Aggregate*, 2024, e540.
25 K. Wei, Y. Wu, X. Zheng, L. Ouyang, G. Ma, C. Ji and M. Yin, A light-triggered J-aggregation-regulated therapy conversion: from photodynamic/photothermal therapy to long-lasting

chemodynamic therapy for effective tumor ablation, *Angew. Chem., Int. Ed.*, 2024, e202404395.
26 C. Ji, L. Lai, P. Li, Z. Wu, W. Cheng and M. Yin, Organic dye assemblies with aggregation-induced photophysical changes and their bio-applications, *Aggregate*, 2021, **2**, e39.
27 V. N. Nguyen, Y. Yan, J. Zhao and J. Yoon, Heavy-atom-free photosensitizers: from molecular design to applications in the photodynamic therapy of cancer, *Acc. Chem. Res.*, 2021, **54**, 207–220.
28 Y. Xiao, X. Huang, J. Feng, Z. Ni, L. Gai, X. Xiao, X. Sui and H. Lu, A simple route toward triplet-forming thionated BODIPY-based photosensitizers, *Dyes Pigm.*, 2022, **200**, 110167.
29 V. N. Nguyen, S. J. Park, S. Qi, J. Ha, S. Heo, Y. Yim, G. Baek, C. S. Lim, D. J. Lee, H. M. Kim and J. Yoon, Design and synthesis of efficient heavy-atom-free photosensitizers for photodynamic therapy of cancer, *Chem. Commun.*, 2020, **56**, 11489–11492.
30 J. Tang, L. Wang, A. Loredo, C. Cole and H. Xiao, Single-atom replacement as a general approach towards visible-light/near-infrared heavy-atom-free photosensitizers for photodynamic therapy, *Chem. Sci.*, 2020, **11**, 6701–6708.
31 V. N. Nguyen, S. Qi, S. Kim, N. Kwon, G. Kim, Y. Yim, S. Park and J. Yoon, An Emerging Molecular design approach to heavy-atom-free photosensitizers for enhanced photodynamic therapy under hypoxia, *J. Am. Chem. Soc.*, 2019, **141**, 16243–16248.
32 V. N. Nguyen, Y. Yim, S. Kim, B. Ryu, K. Swamy, G. Kim, N. Kwon, C. Y. Kim, S. Park and J. Yoon, Molecular design of highly efficient heavy-atom-free triplet BODIPY derivatives for photodynamic therapy and bioimaging, *Angew. Chem., Int. Ed.*, 2020, **59**, 8957–8962.
33 S. Mai, M. Pollum, L. Martinez-Fernandez, N. Dunn, P. Marquetand, I. Corral, C. E. Crespo-Hernandez and L. Gonzalez, The origin of efficient triplet state population in sulfur-substituted nucleobases, *Nat. Commun.*, 2016, **7**, 13077.
34 V.-N. Nguyen, G. Baek, S. Qi, S. Heo, Y. Yim and J. Yoon, A lysosome-localized thionaphthalimide as a potential heavy-atom-free photosensitizer for selective photodynamic therapy, *Dyes Pigm.*, 2020, **177**, 108265.
35 L. A. Ortiz-Rodriguez, S. J. Hoehn, A. Loredo, L. Wang, H. Xiao and C. E. Crespo-Hernandez, Electronic relaxation pathways in heavy-atom-free photosensitizers absorbing near-infrared radiation and exhibiting high yields of singlet oxygen generation, *J. Am. Chem. Soc.*, 2021, **143**, 2676–2681.
36 Z. Liu, Y. Gao, X. Jin, Q. Deng, Z. Yin, S. Tong, W. Qing and Y. Huang, Regioisomer-manipulating thio-perylenediimide nanoagents for photothermal/photodynamic theranostics, *J. Mater. Chem. B*, 2020, **8**, 5535–5544.
37 H. Abrahamse and M. R. Hamblin, New photosensitizers for photodynamic therapy, *Biochem. J.*, 2016, **473**, 347–364.
38 M. Zhu, H. Zhang, G. Ran, Y. Yao, Z. S. Yang, Y. Ning, Y. Yu, R. Zhang, X. X. Peng and J. Wu, Bioinspired design of seco-chlorin photosensitizers to overcome phototoxic effects in photodynamic therapy, *Angew. Chem., Int. Ed.*, 2022, **61**, e202204330.
39 Y. Ning, G. Q. Jin and J. L. Zhang, Porpholactone chemistry: an emerging approach to bioinspired photosensitizers with tunable near-infrared photophysical properties, *Acc. Chem. Res.*, 2019, **52**, 2620–2633.
40 Y. Ning, X. S. Ke, J. Y. Hu, Y. W. Liu, F. Ma, H. L. Sun and J. L. Zhang, Bioinspired orientation of beta-substituents on porphyrin antenna ligands switches ytterbium(III) NIR emission with thermosensitivity, *Inorg. Chem.*, 2017, **56**, 1897–1905.
41 X. S. Ke, Y. Chang, J. Z. Chen, J. Tian, J. Mack, X. Cheng, Z. Shen and J. L. Zhang, Porphodilactones as synthetic chlorophylls: relative orientation of beta-substituents on a pyrrolic ring tunes NIR absorption, *J. Am. Chem. Soc.*, 2014, **136**, 9598–9607.
42 Y. Yu, B. Czepukojc, C. Jacob, Y. Jiang, M. Zeller, C. Bruckner and J. L. Zhang, Porphothionolactones: synthesis, structure, physical, and chemical properties of a chemodosimeter for hypochlorite, *Org. Biomol. Chem.*, 2013, **11**, 4613–4621.
43 H. Zhang, J. H. Wu, H. Z. Xue, R. Zhang, Z. S. Yang, S. Gao and J. L. Zhang, Biomimetically constructing a hypoxia-activated programmable phototheranostics at the molecular level, *Chem. Sci.*, 2022, **13**, 8979–8988.
44 H. Khatoon and E. Abdulmalek, A focused review of synthetic applications of Lawesson's reagent in organic synthesis, *Molecules*, 2021, **26**, 6937.
45 J. Sun, E. Zhao, J. Liang, H. Li, S. Zhao, G. Wang, X. Gu and B. Z. Tang, Diradical-featured organic small-molecule photothermal material with high-spin state in dimers for ultra-broadband solar energy harvesting, *Adv. Mater.*, 2022, **34**, 2108048.
46 Y. L. Lee, Y. T. Chou, B. K. Su, C. C. Wu, C. H. Wang, K. H. Chang, J. A. Ho and P. T. Chou, Comprehensive thione-derived perylene diimides and their bio-conjugation for simultaneous imaging, tracking, and targeted photodynamic therapy, *J. Am. Chem. Soc.*, 2022, **144**, 17249–17260.
47 B. A. Llewellyn, E. S. Davies, C. R. Pfeiffer, M. Cooper, W. Lewis and N. R. Champness, Thionated perylene diimides with intense absorbance in the near-IR, *Chem. Commun.*, 2016, **52**, 2099–2102.
48 J.-Y. Hu, Z.-Y. Wu, K. Chai, Z.-S. Yang, Y.-S. Meng, Y. Ning, J. Zhang and J.-L. Zhang, β-Fluorinated porpholactones and metal complexes: synthesis, characterization and some spectroscopic studies, *Inorg. Chem. Front.*, 2017, **4**, 1539–1545.
49 L. A. Ortiz-Rodriguez and C. E. Crespo-Hernandez, Thionated organic compounds as emerging heavy-atom-free photodynamic therapy agents, *Chem. Sci.*, 2020, **11**, 11113–11123.
50 K. Cai, J. Xie and D. Zhao, NIR J-aggregates of hydroazaheptacene tetraimides, *J. Am. Chem. Soc.*, 2013, **136**, 28–31.
51 Y. Wang, G. Xia, M. Tan, M. Wang, Y. Li and H. Wang, H-dimeric nanospheres of amphipathic squaraine dye with

an 81.2% photothermal conversion efficiency for photothermal therapy, *Adv. Funct. Mater.*, 2022, **32**, 2113098.

52 S. Wang, W. Wu, P. Manghnani, S. Xu, Y. Wang, C. C. Goh, L. G. Ng and B. Liu, Polymerization-enhanced two-photon photosensitization for precise photodynamic therapy, *ACS Nano*, 2019, **13**, 3095–3105.

53 S. Yang, J. Zhang, Z. Zhang, R. Zhang, X. Ou, W. Xu, M. Kang, X. Li, D. Yan, R. T. K. Kwok, J. Sun, J. W. Y. Lam, D. Wang and B. Z. Tang, More Is Better: Dual-acceptor engineering for constructing second near-infrared aggregation-induced emission luminogens to boost multimodal phototheranostics, *J. Am. Chem. Soc.*, 2023, **145**, 22776–22787.

54 Y. Yao, G. Ran, C. L. Hou, R. Zhang, D. N. Mangel, Z. S. Yang, M. Zhu, W. Zhang, J. Zhang, J. L. Sessler, S. Gao and J. L. Zhang, Nonaromatic organonickel(II) phototheranostics, *J. Am. Chem. Soc.*, 2022, **144**, 7346–7356.

55 M. Li, W. Sun, R. Tian, J. Cao, Y. Tian, B. Gurram, J. Fan and X. Peng, Smart J-aggregate of cyanine photosensitizer with the ability to target tumor and enhance photodynamic therapy efficacy, *Biomaterials*, 2021, **269**, 120532.

56 J. Zhang, S. Mukamel and J. Jiang, Aggregation-induced intersystem crossing: rational design for phosphorescence manipulation, *J. Phys. Chem. B*, 2020, **124**, 2238–2244.

57 Y.-F. Kang, W.-K. Chen, K.-X. Teng, L.-Y. Wang, X.-C. Xu, L.-Y. Niu, G. Cui and Q.-Z. Yang, Aggregation turns BODIPY fluorophores into photosensitizers: reversibly switching intersystem crossing on and off for smart photodynamic therapy, *CCS Chem.*, 2022, **4**, 3516–3528.

58 H. Yuan, Z. Han, Y. Chen, F. Qi, H. Fang, Z. Guo, S. Zhang and W. He, Ferroptosis photoinduced by new cyclometalated iridium (III) complexes and its synergism with apoptosis in tumor cell inhibition, *Angew. Chem., Int. Ed.*, 2021, **133**, 8255–8262.

59 Y. Zhao, C. Yu, Y. Yu, X. Wei, X. Duan, X. Dai and X. Zhang, Bioinspired heteromultivalent ligand-decorated nanotherapeutic for enhanced photothermal and photodynamic therapy of antibiotic-resistant bacterial pneumonia, *ACS Appl. Mater. Interfaces*, 2019, **11**, 39648–39661.

60 Y. Yuan, C. J. Zhang, M. Gao, R. Zhang, B. Z. Tang and B. Liu, Specific light-up bioprobe with aggregation-induced emission and activatable photoactivity for the targeted and image-guided photodynamic ablation of cancer cells, *Angew. Chem., Int. Ed.*, 2014, **54**, 1780–1786.